Applied Catalysis A, General 708 (2025) 120571

Contents lists available at ScienceDirect

Applied Catalysis A, General

journal homepage: www.elsevier.com/locate/apcata

Experimental and microkinetic investigation of thermo-catalytic ammonia decomposition over a Ba-promoted Ru/Ni-BCZY catalyst for use in ammonia-fed protonic ceramic cells

Sadaf Davari [a,1], Rinu Chacko [a,2], Tim Bastek [a,3], Patrick Lott [a,4], Julian Dailly [b,5], Sofia Angeli [c,6], Olaf Deutschmann [a,c,*,7]

[a] Institute for Chemical Technology and Polymer Chemistry (ITCP), Karlsruhe Institute of Technology (KIT), Engesserstr. 20, Karlsruhe 76131, Germany
[b] European Institute for Energy Research (EIFER), Emmy-Noether-Straße 11, Karlsruhe 76131, Germany
[c] Institute of Catalysis Research and Technology (IKFT), Karlsruhe Institute of Technology (KIT), Hermann-von-Helmholtz-Platz 1, Eggenstein-Leopoldshafen 76344, Germany

ARTICLE INFO

Keywords:
Ammonia decomposition
Ru catalyst
Ni-BCZY
Hydrogen production/generation
Protonic Ceramic Cell
Thermo-catalytic experiments
Microkinetic modeling

ABSTRACT

Direct ammonia-fed Protonic Ceramic Cells (NH_3-PCC) hold great promise for efficient energy generation, since ammonia can be used directly as fuel at the anode without the need of prior cracking to hydrogen. This study evaluates the catalytic activity of barium-promoted ruthenium catalysts supported on Ni-BCZY cermet particles in a packed-bed reactor, and provides a microkinetic model for simulation of the thermo-catalytic ammonia decomposition reaction. Among the catalysts tested, the 0.5 wt% Ru and 1 wt% Ba supported on a Ni-BCZY cermet exhibited the best performance, requiring less active material. The addition of Ru and Ba improved the catalytic activity of the bare Ni-BCZY cermet, which also shows catalytic activity due to Ni active sites. A new set of microkinetic model parameters is presented, combining Ba-promoted ruthenium and nickel surface steps. This model was used to conduct a parametric simulation, providing insights into the impact of the operating conditions.

1. Introduction

In pursuit of sustainable energy generation, hydrogen (H_2) is considered to be particularly promising as a carbon-free energy carrier. Although currently H_2 is produced primarily from fossil resources, i.e., through steam reforming of natural gas [1–3], viable alternatives for hydrogen generation include using technologies that rely on renewable energy such as electrolysis,[4,5] or methane and biogas pyrolysis [6–11]. When replacing fossil fuels with green hydrogen, not only is the selection of appropriate methods for H_2 production and storage of utmost importance [12], but also the establishment of a suitable large-scale hydrogen carrier [13]. To date, various H_2 carriers are under consideration, such as metal or chemical hydrides, liquid organic hydrogen carriers (LOHC), and porous structures in which hydrogen adsorbs via physisorption [14–16]. Ammonia (NH_3) is another prospective hydrogen carrier; in comparison to H_2, it can be liquified at lower pressure, has a higher volumetric energy density (in liquified form), and is easier to store and transport due to its lower vapor pressure, higher boiling point, and reduced flammability [17]. Since NH_3 is the second most produced chemical in the world, the infrastructure for

* Corresponding author at: Institute for Chemical Technology and Polymer Chemistry (ITCP), Karlsruhe Institute of Technology (KIT), Engesserstr. 20, Karlsruhe 76131, Germany.
E-mail addresses: sadaf.davari@kit.edu (S. Davari), rinu.chacko@kit.edu (R. Chacko), tim.bastek@cse-institut.de (T. Bastek), patrick.lott@kit.edu (P. Lott), Julian.Dailly@eifer.org (J. Dailly), sofia.angeli@kit.edu (S. Angeli), deutschmann@kit.edu (O. Deutschmann).
[1] https://orcid.org/0009-0001-5883-7247
[2] https://orcid.org/0009-0007-2416-1369
[3] CSE Center of Safety Excellence gGmbH, Joseph-von-Fraunhofer-Str. 9, 76327, Pfinztal, Germany.
[4] https://orcid.org/0000-0001-8683-2155
[5] https://orcid.org/0000-0002-4853-3661
[6] https://orcid.org/0000-0001-8623-047X
[7] https://orcid.org/0000-0001-9211-7529

https://doi.org/10.1016/j.apcata.2025.120571
Received 3 June 2025; Received in revised form 11 August 2025; Accepted 13 September 2025
Available online 15 September 2025

NH_3 production, storage, and transportation is well established worldwide [18,19]. However, efficient decomposition of NH_3 is a prerequisite for its use as a H_2 carrier.

Ammonia-fed Protonic Ceramic Cells (NH_3-PCC) allow the direct use of NH_3 as fuel for energy generation [20–23]. Unlike solid oxide cells (SOCs) which use oxygen ion (O^{2-}) conducting electrolytes, PCCs use materials that conduct protons (H^+) and thus have a lower activation energy. This results in lower operating temperatures than SOCs and avoids fuel dilution at the anode when operated in the fuel cell mode with hydrogen as fuel [24,25]. Proton-conducting electrolytes, such as Y-doped $BaCeO_3$-$BaZrO_3$ solid oxides (BCZY), are increasingly used for their excellent H^+ conductivity [26,27]. Due to the importance of material selection in the structure of electrochemical setups, many studies have focused on identifying useful materials and developing performance-improvement strategies [28–30]. A common method to improve stability and performance is to mix metals with conductive electrolyte materials, forming hybrid composites called cermets that increase thermal durability and the number of active sites within the cell [22,31,32]. Therefore, adding nickel (Ni) to the ceramic BCZY [29,33], makes Ni-BCZY a popular choice for use as anode for intermediate-temperature applications [21,22,34]. Since NH_3 decomposition is an endothermic reaction, high temperatures are required for efficient decomposition, typically between 773 K and 1173 K (Eq. 1) [15,35–37]. Therefore, considerable efforts have been reported in literature to study the thermo-catalytic decomposition of ammonia in the presence of metals [18,36–41].

$$2NH_3 \rightleftharpoons N_2 + 3H_2 \rightarrow \Delta H^{298K} = 92.44 kJmol^{-1} \quad (1)$$

Catalysts based on ruthenium (Ru) typically exhibit the highest activity for NH_3 decomposition [41–43]. Since the usage of Ru in commercial applications is limited by its relatively high cost, many studies on the optimization of catalysts [40,44–46], promoters [47–49], and support materials [49–51], as well as the establishment of efficient reactor configurations [40,52,53], have been conducted. According to Zhang et al. [54], barium (Ba) has a thermal stabilizing effect on the Ru catalyst and was shown to act as a promoter for ammonia synthesis. In addition, Ni has also been shown to exhibit high activity for ammonia decomposition [37,55–57], hence its presence in the anode could enhance catalytic activity, and merits further research.

The present work investigates the Ru-catalyzed decomposition of NH_3 over Ni-based cermet supports in a packed-bed reactor for application in PCC setups. The catalyst performance data, supplemented by characterization measurements from scanning electron microscopy (SEM) and energy-dispersive X-ray spectroscopy (EDXS), are utilized to develop and validate a microkinetic model for catalytic ammonia decomposition over a Ba-promoted Ru/Ni-BCZY catalyst that also considers the activity of the metallic nickel present in the cermet support along with ruthenium. Finally, the proposed microkinetic model is used to investigate the surface dynamics and perform a parametric study to offer insights on the impact of operating conditions on the catalytic performance.

2. Experimental procedure

2.1. Catalyst preparation

Ni-based cermet material that are typically used in PCCs and SOCs were prepared by means of tape casting and subsequent sintering. Two different tapes were prepared by mixing either $BaCe_{0.8}Zr_{0.1}Y_{0.1}O_{3-\delta}$ (BCZY811; CerPoTech A.S.) or yttria-stabilized zirconia (8-YSZ; Tosoh Europe B.V.) powder with graphite (TimCal), ethanol, and methyl ethyl ketone (MEK) as solvents and dispersant. For all cermet-based samples, the BCZY or YSZ powder was additionally mixed with NiO powder (J.T. Baker®) in a weight ratio of 40:60. After mixing the resulting slurry for 24 h in a TURBULA® 3D shaker mixer (type T2F, WAB), polyvinyl butyral (PVB) and two plasticizers (PEG and TEG-EH by Eastman) were added. At that point the solution was mixed once again for 3 h before it was rested for 24 h, and then de-airing was conducted under vacuum. Subsequently, a ZAA 2300 automatic film applicator coater (Zehnter GmbH) was used to cast the slurry onto a silicone-coated PET film. In order to remove the solvents, the resulting tape was then dried for 12 h at room temperature and for 10 min at 773 K. Analogous to PCC fabrication [58], the tapes were finally sintered for 9 h at 1673 K. To ensure the creation of open pores during the decomposition of organic components and graphite, and to minimize crack-formation as a result of thermal stress, the heating and cooling ramps for the sintering step were chosen to be 1 K min^{-1} and 3 K min^{-1}, respectively.

The sintered tapes crushed to a fine powder were used as support material for the catalysts. This approach ensures that the material properties during packed-bed testing are analogous to those in a PCC configuration. Ru and/or Ba were deposited by means of incipient wetness impregnation (IWI) using an aqueous ruthenium(III)-nitrosyl-nitrate solution (Alfa Aesar) and an aqueous Ba-containing precursor solution that was prepared by dissolving $Ba(NO_3)_2$ powder (Alfa Aesar) in deionized water. Due to the relatively low pore volume of the cermet-based support material, the precursor solution was added stepwise with 100 µL per step and was subsequently dried at 348 K for 15 min until the desired amount of Ba and/or Ru was added. It should be mentioned that, in this formulation, the additional catalysts Ru and Ba are introduced as nanoparticles supported on the crushed cermet material and are not incorporated into the bulk of the proton-conducting ceramic. The nitrates were decomposed during calcination for 5 h at 873 K in static air, and the prepared catalysts were granulated to a particle fraction of 120–250 µm. Table 1 provides an overview of the prepared catalysts studied in this work.

2.2. Catalyst characterization

A BELSORP Mini II analyzer (MicrotracBEL) was used to obtain nitrogen adsorption-desorption isotherms at 77 K. To remove any adsorbed contaminants, the catalyst samples were degassed for two hours at 573 K before the actual physisorption test. Using the adsorption data in the range of 0–0.5 relative pressure, the specific surface area was calculated according to the Brunauer-Emmett-Teller (BET) method.

The grain size was investigated using Scanning Electron Microscopy (SEM). A QuantaTM 250 FEG running at 20 kV accelerating voltage was used to obtain the SEM images. The sample's composition and average nanoparticle size were estimated using SEM imaging and Energy-Dispersive X-ray Spectroscopy (EDX), which also revealed information about the sample's nanoparticle size and structural integrity.

Temperature-programmed reduction (TPR) was conducted to evaluate the reducibility of the catalyst and to provide insight into the strength of the interaction between the active metal species and the support. The TPR experiments were performed using approximately 0.1 g of the powdered catalyst, which were placed in a quartz reactor and heated from room temperature to 1223 K at a heating rate of 10 K min^{-1} in a mixture of 10 % H_2 in Ar (50 mL min^{-1}). Simultaneously, the H_2 consumption was monitored using a thermal conductivity detector (TCD).

The dispersion of Ni on the BCZY support was measured via H_2

Table 1
Overview of the six prepared catalysts (nominal compositions). BCZY: $BaCe_{0.8}Zr_{0.1}Y_{0.1}O_{3-\delta}$, YSZ: ZrO_2 • 0.03 mol% Y_2O_3.

Catalyst	Ru in wt%	Ba in wt%
Ni-BCZY cermet	-	-
1Ru/Ni-BCZY	1.0	-
0.5Ru/1Ba/ Ni-BCZY	0.5	1.0
0.5Ru/0.5Ba/ Ni-BCZY	0.5	0.5
1Ru/1Ba/YSZ	1.0	1.0
1Ru/1Ba/Ni-YSZ	1.0	1.0

temperature-programmed desorption (TPD-H_2). As a pretreatment, 100 mg of the sample were heated to 923 K under 40 mL min^{-1} of Ar flow followed by reduction under 11 % H_2/Ar for 1 h at 650 °C. After reduction, the sample was flushed in Ar flow (40 mL min^{-1}) at 923 K for 0.5 h and subsequently cooled down to room temperature and flushed until H_2 signal is stabilized. The chemisorption step took place under a flow of 10 % H_2/Ar for 1 h at 298 K (total flow 50 mL min^{-1}). The temperature of adsorption was selected in order to minimize the effect of hydrogen spillover in the support. The temperature programmed desorption was carried out in a heating rate of 10 K min^{-1} until the temperature of 1123 K. The integrated peak of desorbed hydrogen was compared to that of reference H_2 pulses. The atomic ratio H:M of 1:1 was considered for the calculation of the metal dispersion. The specific surface area of metal for each catalyst was based on the consideration that the area occupied by a surface metal atom for Ni is 6.51 $Å^2$ [59].

2.3. Thermo-catalytic experiments

The catalytic activity of the prepared catalyst samples was evaluated in a lab-scale catalyst testing unit as described elsewhere [60]. For the tests, a quartz glass tubular reactor (inner diameter 0.8 cm, length 100 cm) loaded with 300 mg of the catalyst granulate mixed with 700 mg of silica particles (both with a sieve fraction of 120–250 μm), resulting in a catalyst bed length of approx. 1.2 cm. The bed was fixed by two quartz wool plugs and the reactor was placed in a furnace. The gases were fed to the reactor through mass flow controllers (Bronkhorst). The catalyst bed temperature during the reaction was monitored by two thermocouples (type N), which were positioned approximately 2 mm up- and downstream of the catalyst bed, while a Fourier-transform infrared (FTIR) spectrometer (MG2030, MKS Instruments) was used to continuously analyze the effluent gas stream.

Each catalytic test started with 1.5 h of pretreatment at 873 K in 5 % H_2 and balance in Ar. After cooling to 473 K and purging for 1 h in pure Ar to remove all H_2 from the reactor, the performance tests were conducted at 1 bar with different NH_3 concentrations (500 ppm, 1000 ppm, and 3000 ppm NH_3) balanced in Ar. For this, the temperature was ramped to 873 K with a rate of 2 K min^{-1}, and a gas hourly space velocity (GSHV) of 50,000 h^{-1} was chosen.

3. Modeling approach and numerical simulation

3.1. Numerical simulations

The DETCHEM^{PBR} code [10], which is part of the DETCHEM [61] simulation package, was utilized to perform the numerical simulations of the packed-bed reactor model, combined with detailed kinetic models. Eqs. 2 and 3 represent the set of governing equations solved in DETCHEM^{PBR}, under the assumptions of negligible axial diffusion and constant flow properties in the radial direction.

$$\frac{d(\rho u)}{dz} = a_v \sum_{i \in \mathscr{S}_g} \dot{s}_i M_i \tag{2}$$

$$\rho u \frac{d(Y_i)}{dz} + Y_i \; a_v \sum_{i \in \mathscr{S}_g} \dot{s}_i M_i = M_i (a_v \; \dot{s}_i + \dot{\omega}_i \varepsilon) \tag{3}$$

Herein, ρ is the density, u is the superficial gas velocity, z is the axial coordinate, a_v is the ratio of particle surface area to reactor volume, $\dot{s}_i$ is the surface reaction rate of species i, M_i is the species molar mass, Y_i is the species mass fraction in the gas-phase, $\dot{\omega}_i$ is the gas-phase reaction rate, ε is the porosity of the packed-bed, and $\mathscr{S}_g$ is the set of all gas-phase species.

The external fluid-solid mass transfer effect was also considered for a more precise estimation of the reaction rates at the catalyst surface and modeled through Eqs. 4 and 5.

$$\dot{s}_i M_i = k_{fs,\;i} \; (c_{i,f} - \; c_{i,\;s}) \tag{4}$$

$$k_{fs,\;i} = \frac{Sh D_i}{d_p} \tag{5}$$

Herein, $k_{fs,i}$ is the fluid-solid mass transfer coefficient, $c_{i,f}$ is the species concentration in the fluid-phase, $c_{i,s}$ is the species concentration at the catalyst surface, Sh is the Sherwood number, D_i is the species diffusion coefficient, and d_p is the particle diameter. The bed porosity is calculated using the Pushnov approximation in Eq. 6 correlating the particle and reactor diameter (d_p and $D_{reactor}$) for spherical particles (A_p = 1.0, B_p= 0.375, and n = 2) [62].

$$\varepsilon = \frac{A_p}{\left(\frac{D_{reactor}}{d_p}\right)^n} + \; B_p \tag{6}$$

The CaRMeN (Catalytic Reaction Mechanisms Network) software was used to accelerate the simulation workflow and for validation of the numerical simulations with experimental data [61,63,64].

3.2. Kinetic model

The surface reaction rates for species i are calculated through Eq. 7 where the rate constant k_k for the k^{th} reaction is modeled using the modified Arrhenius expression according to Eq. 8, which in contrast to the typical Arrhenius expression also includes the coverage-dependency parameter ϵ_i on the activation energy due to the coverage θ_i for the species i.

$$\dot{s}_i = F_{cat/geo} \sum_{k \in \mathscr{R}_s} \theta k_k \prod_{j \in \mathscr{S}_g \cup \mathscr{S}_s} c_j^{\nu'_{jk}} \tag{7}$$

$$k_k = A_k \; T^{\beta_k} \exp\left(-\frac{E_{a_k}}{RT}\right) \prod_{i \in \mathscr{S}_s} \exp\left(\frac{\epsilon_{i,k}\theta_i}{RT}\right) \tag{8}$$

$$\theta_i = \frac{c_i \sigma_i}{\Gamma} \tag{9}$$

Herein, $\mathscr{R}_S$and $\mathscr{S}_S$ are the set of all surface reactions and species, respectively, ν_{ik} is the stoichiometric coefficient of species i for reaction k, A_k is the pre-exponential factor, T is the temperature, β_k is the temperature-dependency parameter, E_{a_k} is the activation energy, and R is the universal gas constant (R = 8.314 k mol^{-1} K^{-1}). The surface coverages θ_i are estimated under the mean field approximation using the surface concentration of species i (c_i), the number of occupied adsorption sites per adsorbed molecule i (σ_i), and the surface site density Γ. The DETCHEM^{SURFPROBE} code was used to calculated the surface coverages and fluxes over the catalytic surface [61].

$F_{cat/geo}$ correlates the actual catalytically active surface area A_{cat} to the geometrical area A_{geo} of the particles. A_{cat} is calculated under the assumption that half of the spherical metal nanoparticle surface is exposed on the surface.

$$F_{cat/geo} = \frac{A_{cat}}{A_{geo}} \tag{10}$$

$$A_{geo} = N_p \; 4\pi\left(\frac{d_p}{2}\right)^2 \tag{11}$$

$$A_{cat} = \; 0.5 \; \frac{m_{metal}}{\rho_{metal}} \; \frac{6}{d_{np}} \tag{12}$$

Herein, N_p is the total number of particles in the catalyst bed, d_p is the diameter of the particle, m_{metal} is the active metal catalyst mass calculated based on the catalyst loading, ρ_{metal} is the density of the active metal catalyst, and d_{np} is the diameter of the nanoparticle. Additionally, the rates of the adsorption reactions are modeled using Eq. 13 in terms of sticking coefficients, S_i^0, which represents the probability that a gas-phase molecule will adsorb when it collides with the surface.

$$\dot{s}_i = S_i^0 \prod_{j \in Ss} \theta_j^{\nu' jk} \sqrt{\frac{RT}{2\pi M_i}} c_i \tag{13}$$

3.3. Microkinetic model and automated optimization procedure of the parameters

The mechanism for ammonia synthesis has been widely studied in the literature considering various active catalysts, promoters and supports [65–69]. In 1996, Hinrichsen et al. [70] established a microkinetic model for NH_3 synthesis consisting of 12 elementary steps encompassing N_2 and H_2 dissociative adsorption/desorption, sequential hydrogen abstractions, and NH_3 adsorption/desorption over a Cs/Ru-MgO catalyst, wherein the kinetic parameters for the N_2 desorption step were obtained via temperature-programmed desorption experiments. In this work, to model the experimental data for ruthenium catalyst samples, we use the microkinetic model and thermodynamically consistent kinetic parameters including coverage-dependent activation energies proposed by Zhang et al. [54] for a Ba-promoted Ru catalyst supported on YSZ; these data were validated with experiments for ammonia synthesis at various operating conditions. In accordance with the principle of microscopic reversibility, the mechanism for ammonia synthesis can also be used to describe ammonia decomposition. Additionally, to model the Ni-BCZY cermet sample, the microkinetic model proposed by Zhu et al. [71] is used, that investigated ammonia decomposition on a dual-channel protonic-ceramic fuel cell (PCFC) over a membrane electrode. It is to be noted that in both of these models, the reaction steps considered are as proposed by Hinrichsen et al. [70]; however, the individual rate coefficients were modified to fit the experimental observations.

In the present work as well, the kinetic parameters needed to be optimized to match the experimental observations for selected samples. This was accomplished using the automated optimization procedure for detailed microkinetic models based on the Basin-Hopping algorithm, a global stochastic optimizer. The general approach for the automated optimization procedure is described in detail in an earlier work [72]. The algorithm stochastically explores the high-dimensional kinetic parameter space without relying on gradient information. It combines random perturbations with local minimization using the Nelder-Mead method to identify parameter sets that minimize deviation from experimental data. Only the kinetic parameters of linearly independent reactions are directly optimized at each step [73]. The objective function for the optimization was chosen as the sum of the absolute difference between the experimental data points and the simulated data points over various reactor temperatures T_r as shown in Eq. 14.

$$f(\lambda_j) = \sum\nolimits_r \left| \overline{X}_{NH_3,\ T_r} - X_{NH_3,\ T_r} \right| \tag{14}$$

Herein, λ_j denotes a j-dimensional vector representing the overall kinetic parameters to be optimized for a given microkinetic model, while $\overline{X}_{NH_3,\ T_r}$ and $X_{NH_3,\ T_r}$ indicate the simulated and experimental conversion of NH_3 at a given reactor temperature. It is to be noted that, since the number of parameters to be tuned is large compared to the number of experiments, multiple solutions exist that perform similarly. We report in this work the values that perform reasonably well on the validation data as well as the fitting data. Only the performance data corresponding to the inlet feed concentration of 1000 ppm of NH_3 was used in the objective function during the fitting procedure, while the rest of the experimental data were used for validation of the fitted parameters. The Basin-Hopping iterations and the Nelder-Mead local search iterations were kept as 25 and 200, respectively, to allow a thorough exploration of the kinetic parameter space to obtain the optimal parameters. The step size for the hopping step was kept as 0.05 representing a 5 % change in the parameter value in either direction at each iteration. For maintaining thermodynamic consistency in the entire surface mechanism, the number of degrees of freedom in the combined mechanism is 2 [73]. Therefore, the kinetic parameters associated with the NH_3 desorption step for the Ni surface and the reverse of the dehydrogenation reaction for the Ru surface were calculated at each iteration via DETCHEM^{ADJUST} such that Eq. 15 is satisfied for all pairs of reversible reactions in the model, hereby ensuring thermodynamic consistency throughout the optimization routine [73,74]. This elementary step was chosen through a preliminary sensitivity analysis due to its least sensitivity towards NH_3 conversion. This approach effectively reduces the dimensionality of the parameter space by deterministically calculating dependent parameters.

$$\frac{k_f(T)}{k_r(T)} = \prod\nolimits_i \left(c_i^{\ominus}\right)^{\nu_i} \exp\left(-\frac{\Delta_R G}{RT}\right) \tag{15}$$

Herein, k_f is the forward reaction rate constant, k_r is the rate constant for the reverse reaction, $\Delta_R G$ is the Gibbs free energy change, and $c_i^{\ominus}$ is the concentration of species i at standard conditions.

4. Results and discussion

4.1. Experimental results

Due to their relevance for NH_3-PCC applications, catalyst materials based on BCZY have been studied frequently in the past [25,75,76]. Since in the present study the performance of the catalysts is evaluated thermo-catalytically, tests were also conducted with samples using YSZ ceramic and Ni-YSZ cermet, which serve as reference materials and enable a comparative analysis of the catalytic activity of materials that are commonly used in fuel cell applications. The primary aim was to observe the effect of addition of ruthenium as active metal and barium as promotor on the catalytic activity of the cell materials. Table 2 summarizes the BET surface area of the YSZ powder and the NiO-BCZY support. The cermet-based support exhibits a very low specific surface area of 1.1 $m^2\ g^{-1}$ because the synthesis and processing conditions of cermet materials often involve high-temperature treatments to achieve the necessary structural and compositional characteristics [77,78]. Despite its low surface area, the dense and stable matrix of the cermet support is essential for maintaining the structural integrity and ensuring the efficient conduction of ions and electrons within the fuel cell. Additionally, nickel oxide (NiO) plays an important role [79]. NiO is used as a precursor which, after reduction, forms nickel (Ni) particles within the ceramic matrix that act as active sites for electrochemical reactions with a dispersion of 3.17 %. The combination of Ni with the ceramic material affects the overall catalytic activity and durability of the fuel cell, compensating for the low surface area by potentially providing additional active sites for ammonia decomposition [21,22]. Thus, there exists a trade-off between the specific surface area and the electrical and mechanical properties required in PCC fuel cell applications.

The TPR profile of the Ni-BCZY support, shown in Fig. 1, reveals a single, sharp, symmetrical peak at around 673 K. This sharp peak suggests a straightforward, well-defined reduction process. The BCZY support contributes to moderate stabilization of NiO, enhances reducibility through oxygen vacancies, and improves catalytic performance via structural and electronic effects, making Ni-BCZY effective for intermediate-temperature application [21,22].

The experimentally determined NH3 conversion curves of the various catalysts listed in Table 1 at temperatures ranging from 473 to 873 K for 1000 ppm NH_3 in Ar, are plotted in Fig. 2. The differences in activity amongst the various supported catalyst samples suggest that the support material has a significant impact on catalytic performance. The 1Ru/1Ba/YSZ catalyst is the most active, with an onset temperature of 503 K and full NH_3 conversion at approximately 673 K. The superior

Table 2
BET analysis for NiO-BCZY and YSZ.

Support Material	Specific surface area
NiO-BCZY (Oxidized state)	1.1 $m^2\ g^{-1}$
YSZ	14.1 $m^2\ g^{-1}$

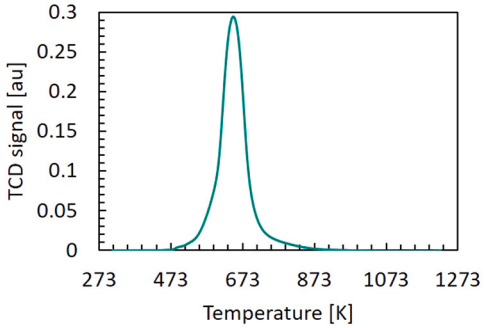

Fig. 1. TPR profile of Ni-BCZY during heating with 10 K min^{-1} in 10 % H_2 in Ar.

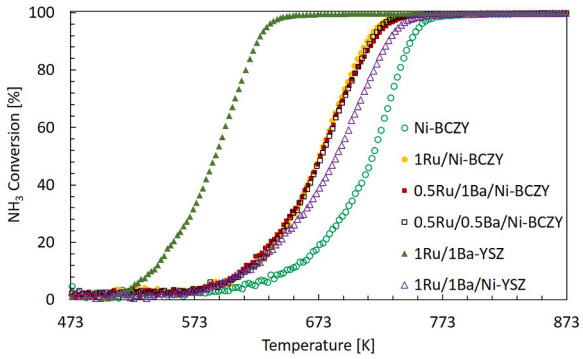

Fig. 2. Catalytic NH_3 decomposition performance of various samples in a packed-bed reactor. Conditions: 1000 ppm NH_3 in Ar; GHSV = 50,000 h^{-1}; ramp rate = 2 K min^{-1}; P = 1 bar.

performance of this sample compared to others is due to the high activity [43] and amount of Ru, the promoting effects of Ba [80], and the higher surface area of the YSZ powder support (Table 2), resulting in better dispersion of the active material [54,81,82]. It has been shown in the literature that YSZ alone exhibits very low activity for ammonia decomposition, while addition of Ni, to form a cermet composite, boosts the activity [32]. However, as shown in Fig. 2 including Ni in the support in the presence of other active metals (1Ru/1Ba/Ni-YSZ catalyst) results in a significant decrease in performance, in spite of having the same content in Ru and Ba. This can be attributed to the Ni accumulated, which forms large particles [32] and leads to a loss of the internal porosity and surface area of the cermet-supported sample compared to the YSZ powder, due to the high sintering temperatures used during the preparation of the cermet support [32,77,78]. The Ni-BCZY sample with no additional ruthenium or barium has the lowest activity compared to other catalyst samples, while the activity is increased by addition of ruthenium alone or in combination with barium, and perform better than the 1Ru/1Ba/Ni-YSZ sample. A prior study has demonstrated that Ni-BCZY is more active than Ni-YSZ for ammonia decomposition, due to its lower tendency to get poisoned by hydrogen [76,83]. Note, that in this context hydrogen poisoning means the hydrogen species cover the surface of the catalyst, occupying the free active sites, and thereby decrease the catalyst's efficiency [84]. The promotor effect of Ba can be observed by comparing the activity of samples with and without barium. The samples containing Ba along with 0.5 wt% Ru (i.e. 0.5Ru/1Ba/-Ni-BCZY and 0.5Ru/0.5Ba/Ni-BCZY) performs at par with the 1Ru/N-i-BCZY sample containing 1 wt% Ru. Table 3 depicts the T_{10} and T_{50} values for each sample, i.e., the temperatures required to achieve 10 % and 50 % conversion of ammonia, respectively. By replacing some of the active noble metal with 1 wt% Ba in the 0.5Ru/1Ba/Ni-BCZY sample, there is a slight improvement in T_{10} and the performance at higher temperatures is very similar to that of 1Ru/Ni-BCZY (Table 3).

Table 3
Temperature for 10 % and 50 % conversion, T_{10} und T_{50}, for each catalyst sample corresponding to the performance data plotted in Fig. 2.

Catalyst sample	T_{10} in K	T_{50} in K
Ni-BCZY	656	717
1Ru/ Ni-BCZY	621	675
0.5Ru/1Ba/ Ni-BCZY	615	675
0.5Ru/0.5Ba/ Ni-BCZY	621	676
1Ru/1Ba-YSZ	536	589
1Ru/1Ba/Ni-YSZ	621	688

Therefore, 0.5Ru/1Ba/Ni-BCZY was selected for further investigation, due to its catalytic performance and potential for usage in NH_3-PCC.

Fig. 3 illustrates the performance of the chosen catalyst, 0.5Ru/1Ba/Ni-BCZY, at three different ammonia inlet concentrations. As the ammonia concentration in the inlet is increased from 500 to 1000 ppm and then to 3000 ppm, the temperature required to achieve 50 % conversion increases from 653 to 674 and subsequently to 695 K. Regardless of the ammonia concentration in the feed, conversion starts at about 523 K and ammonia is fully converted beyond 758 K.

The 0.5Ru/1Ba/Ni-BCZY sample was further characterized via SEM and EDX analysis. Fig. 4 shows the results of SEM measurements under different resolutions. The average diameter of 50 particles was measured to be 241 μm with a standard deviation of 42 μm. The SEM results (Fig. 4c) showed a macro-porous structure with sharp edges that could be due to the high fraction of metallic nickel present after reduction. Fig. 5 depicts the EDX result along with the cropped and masked EDX image by the ImageJ software [85] for analysis (Fig. 5b). The EDX image demonstrates a uniform dispersion of the ruthenium metal, and with 30000x–240000x magnifications individual particles could be identified, and their size distribution was determined to be 4.78 ± 1.16 nm.

4.2. Reactor simulations

Since the experimental data and prior literature studies [32,76] indicate that the cermet support, namely Ni-BCZY with 60 wt% NiO, is catalytically active under the conditions of interest due to the presence of Ni, the kinetic model for catalyst samples supported on Ni-BCZY should also consider the elementary steps on nickel surface sites in addition to ruthenium. Therefore, a microkinetic model combining both surfaces was developed for the 0.5Ru/1Ba/Ni-BCZY sample, which may be utilized for PCC design comprising Ni-BCZY as anode.

As an initial estimate, the reaction steps for the Ni and Ru surfaces with associated kinetic parameters were taken from the microkinetic models for Ni and Ba-promoted Ru catalysts reported by Zhu et al. [71] and Zhang et al. [54], respectively, and a combined mechanism was formulated by including both sets of elementary reaction steps over each metal. The comparison of the simulated data using the initial estimated

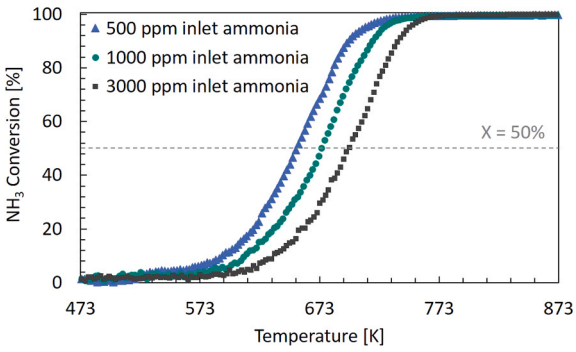

Fig. 3. NH_3 conversion curves for the 0.5Ru/1Ba/Ni-BCZY catalyst. Conditions: 500, 1000, or 3000 ppm NH_3 in Ar; GHSV = 50,000 h^{-1}; ramp rate = 2 K min^{-1}; P = 1 bar.

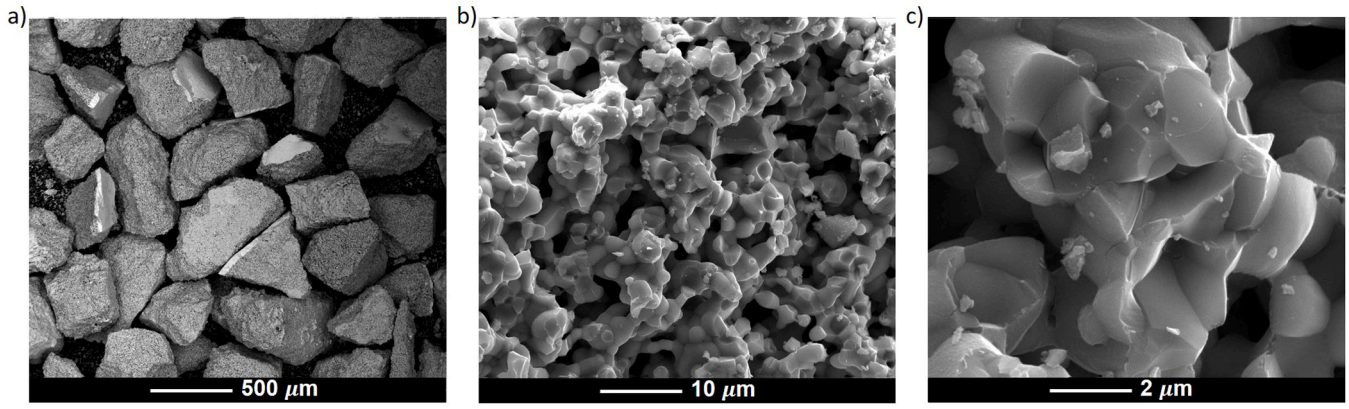

Fig. 4. SEM images of the 0.5Ru/1Ba/Ni-BCZY catalyst with increasing magnification from left to right. a) Image obtained from backscattered electron (BSE) measurements; b) image obtained from secondary electron (SE) measurements; c) image obtained from BSE measurements at higher magnification.

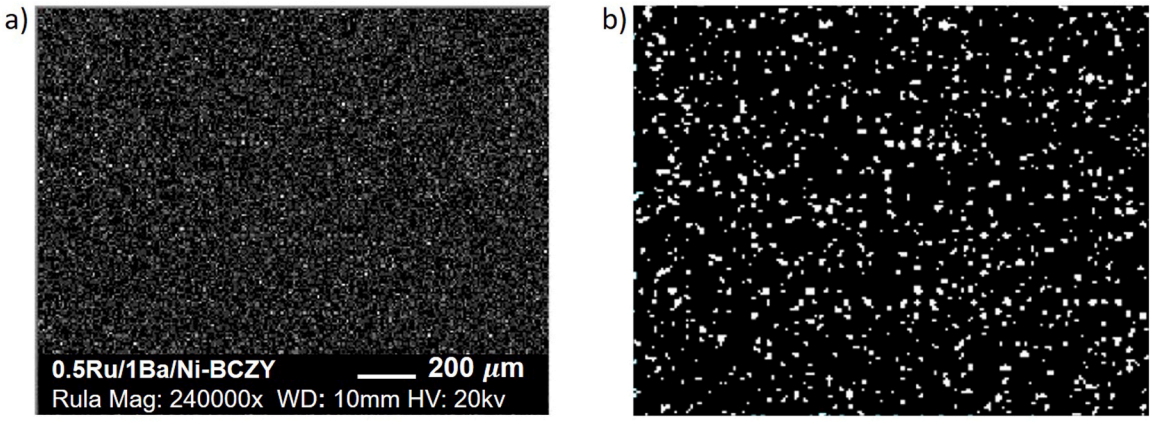

Fig. 5. a) Ru distribution according to EDX analysis of the 0.5Ru/1Ba/Ni-BCZY catalyst; b) ImageJ zoomed in on the clipped and masked EDX image.

parameters along with the experimental data shown earlier in Fig. 3 in the temperature range of 473–873 K can be found in the supplementary material. The nickel dispersion of 3.17 % and the ruthenium nanoparticle size of 4.78 nm, which corresponds to a Ru dispersion of 13.5 % [86], used for the calculation of the catalytically active area, were obtained from H_2-TPD (temperature-programmed desorption) measurements and the EDX analysis, respectively. As expected, the simulations overpredict the experimentally observed performance significantly. This overprediction was probable since the kinetic parameters reported by Zhang et al. [54] were for Ba-promoted Ru supported on YSZ, and the parameters reported by Zhu et al. [71] were validated for Ni supported on $BaZrO_3$. Hence, in order to better understand the Ru activity on a Ni-BCZY support, an accurate prediction of the Ni activity in the cermet support is required.

To this extent, we first performed additional temperature-programmed experiments with a Ru-free Ni-BCZY sample at various concentrations of NH_3. The experimental data and the corresponding numerical simulation results with the Ni-BCZY cermet sample are compared in Fig. 6; note that the original kinetic parameters as reported for a Ni surface by Zhu et al. [71] were used (solid lines). The available active catalyst area is incorporated in the reactor simulations through the calculation of $F_{cat/geo}$ (Eq. 10) based on the characterization data of the Ni-BCZY sample. The overprediction in the simulations, as mentioned above, is because in the study of Zhu et al. [71], the model parameters were fitted using the thermo-catalytic ammonia decomposition experiments over a highly active 40 wt% $Ni/BaZrO_3$ sample taken from Okura et al. [87] Since the $Ni/BaZrO_3$ sample was synthesized by impregnation of Ni on the $BaZrO_3$ ceramic, its microstructure is likely different from the Ni-BCZY cermet used in the present work, therefore the model parameters do not reflect well the experimental observation of low activity. In here, NiO accounts for 60 wt% of the cermet support and undergoes an intense cermet-making process, leading to low porosity (Table 2), with only a small amount of catalytically active Ni accessible on the surface, thereby exhibiting relatively low catalytic activity. In order to accurately describe the Ni-BCZY performance, an optimization of the kinetic parameters for Ni surface reactions was required and performed as described in Section 3.3. The experimental data for 1000 ppm NH_3 was used for fitting the parameters and the data for 500 and 3000 ppm was used for validation of the optimized model. The available active catalyst area through $F_{cat/geo}$ was kept constant throughout the optimization procedure. The simulations with the optimized kinetic parameters shown by dashed lines in Fig. 6, demonstrate a good agreement with the experimental data for 500 ppm and slightly underpredict the performance at 3000 ppm. The better predictions after the optimization of the kinetic parameters highlight that even though the reaction steps considering Ni as the active metal do not change, the kinetic parameters needed to be altered to reflect the effect of the sample morphology.

Moreover, since the kinetic model over the Ru surface of Zhang et al. [54] was developed for a YSZ support, it was necessary to optimize also the parameters associated with the ruthenium reaction steps to reflect the effect of the Ni-BCZY support (procedure described in Section 3.3). Similar to the procedure followed for the Ni-BCZY sample, the data for 1000 ppm NH_3 was used for fitting and the data for 500 and 3000 ppm was used for the validation of the parameters. Fig. 7 shows the comparison of the experimental data on ammonia decomposition over

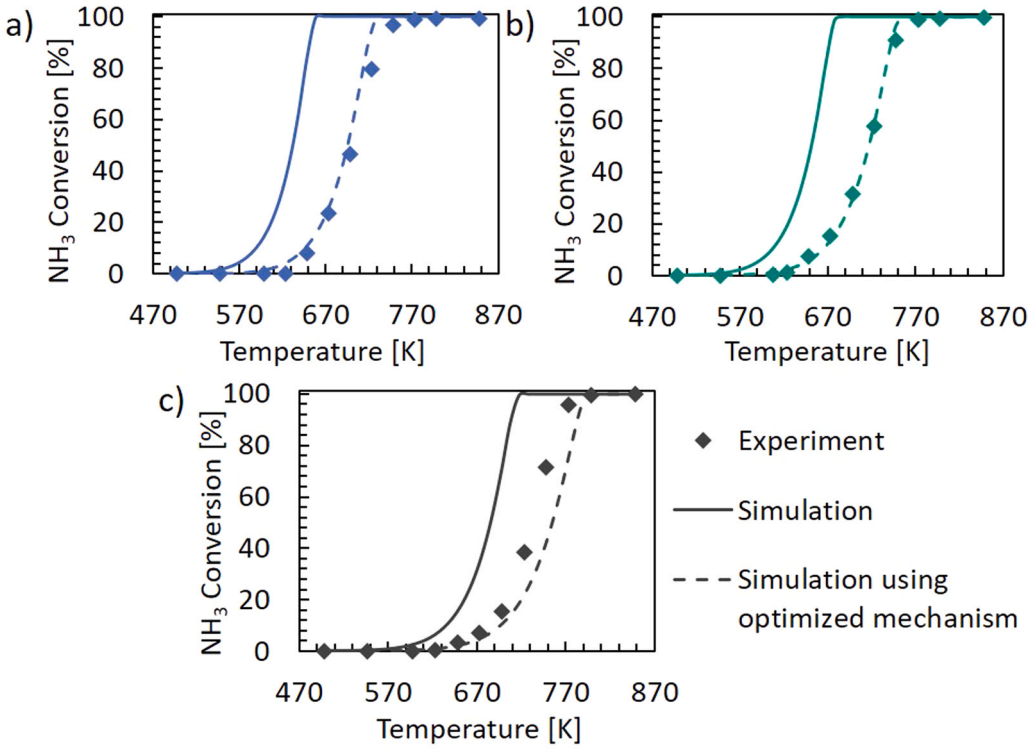

Fig. 6. Comparison between the experimental and simulated NH_3 conversion over Ni-BCZY using original Zhu et al. [71] kinetic parameters (solid lines) and optimized parameters (dashed lines). Conditions: 500 (a), 1000 (b), or 3000 (c) ppm NH_3 in Ar; GHSV = 50,000 h^{-1}; ramp rate = 2 K min^{-1}; P = 1 bar.

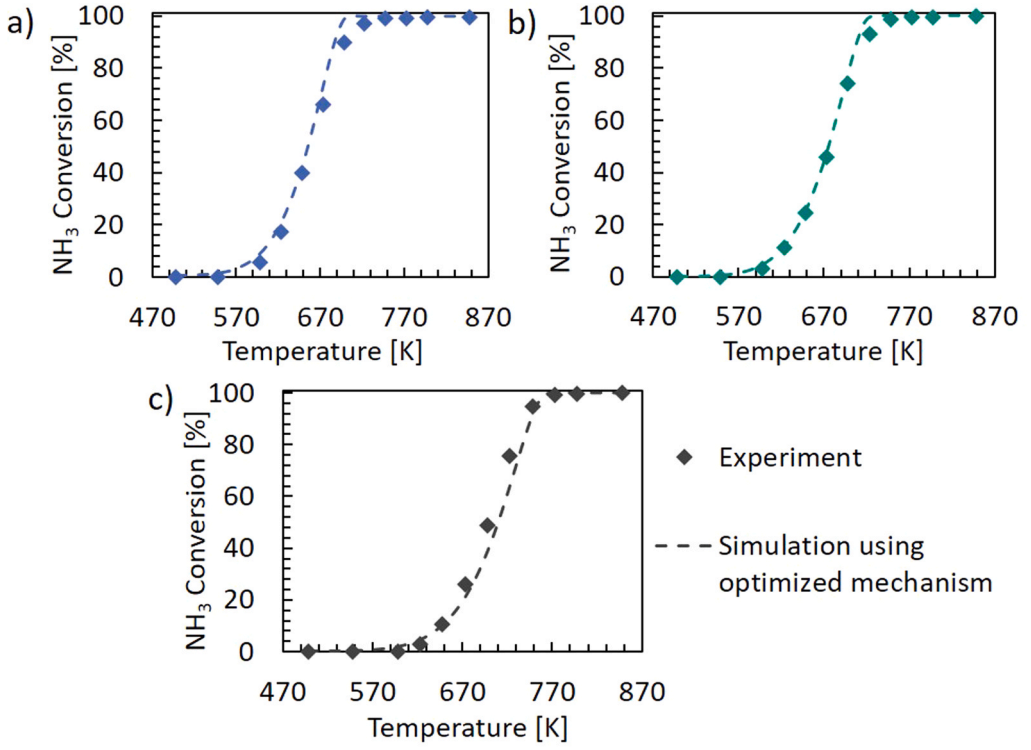

Fig. 7. Comparison between the simulated data using the optimized Ru and Ni surface reaction parameters and the experimental data for 0.5Ru/1Ba/Ni-BCZY. P = 1 bar, GHSV = 50,000 h^{-1}, with varying NH_3 inlet concentration diluted in Ar: a) 500 ppm, b) 1000 ppm, c)3000 ppm.

0.5Ru/1Ba/Ni-BCZY with the data simulated using the dual surface mechanism (c.f. Table 4), comprising the optimized reaction parameters involving the reactions on the ruthenium surface and the previously optimized parameters of the Ni surface reactions. As the figure shows, the optimized model is able to predict the experimental data with a good accuracy for all NH_3 concentrations. A detailed comparison between

Table 4
Thermodynamically consistent detailed kinetic model for Ru/Ba/Ni-BCZY. S_i^0: Sticking Coefficient, A_k: Pre-exponential factor, E_{a_k}: Activation energy, β: Temperature dependency parameter (Eq. 8).

Reaction	S_i^0	A_k [cm,mol, s]	β	E_{a_k} [kJ/mol]
$N_2 + 2\ Ru \rightarrow 2\ N(Ru)$	3.01×10^{-06}	-	0.0	35.87
$2\ N(Ru) \rightarrow 2\ Ru + N_2$	-	2.08×10^{17}	−0.297	$143.70–18.03\theta_{N(Ru)}$
$H_2 + 2\ Ru \rightarrow 2H(Ru)$	3.91×10^{-03}	-	0.0	0.0
$2H(Ru) \rightarrow 2\ Ru + H_2$	-	3.75×10^{20}	0.734	$91.82–1.67\theta_{H(Ru)}$
$NH_3 + Ru \rightarrow NH_3(Ru)$	1.15×10^{-05}	-	0.0	0.0
$NH_3(Ru) \rightarrow Ru + NH_3$	-	2.51×10^{11}	0.087	72.45
$H(Ru) + N(Ru) \rightarrow NH(Ru) + Ru$	-	2.02×10^{22}	−0.380	$101.6–9.02\theta_{N(Ru)}$
$NH(Ru) + Ru \rightarrow H(Ru) + N(Ru)$	-	6.31×10^{19}	0.216	$33.44 + 0.83\theta_{H(Ru)}$
$NH(Ru) + H(Ru) \rightarrow NH_2(Ru) + Ru$	-	5.25×10^{19}	0.100	84.93
$NH_2(Ru) + Ru \rightarrow NH(Ru) + H(Ru)$	-	8.91×10^{19}	−0.085	$15.65 + 0.83\theta_{H(Ru)}$
$NH_2(Ru) + H(Ru) \rightarrow NH_3(Ru) + Ru$	-	3.58×10^{19}	0.081	16.10
$NH_3(Ru) + Ru \rightarrow NH_2(Ru) + H(Ru)$	-	1.36×10^{20}	0.0	$76.90 + 0.83\theta_{H(Ru)}$
$H_2 + 2\ Ni \rightarrow 2H(Ni)$	1.87×10^{-03}	-	0.0	0.0
$2H(Ni) \rightarrow 2\ Ni + H_2$	-	5.92×10^{20}	−0.11	103.94
$NH_3 + Ni \rightarrow NH_3(Ni)$	1.82×10^{-05}	-	−0.097	0.02
$NH_3(Ni) \rightarrow Ni + NH_3$	-	9.89×10^{12}	−0.825	50.35
$N_2 + 2\ Ni \rightarrow 2\ N(Ni)$	1.43×10^{-06}	-	0.0	53.95
$2\ N(Ni) \rightarrow 2Ni + N_2$	-	1.83×10^{16}	−0.136	129.43
$NH_3(Ni) + Ni \rightarrow NH_2(Ni) + H(Ni)$	-	1.84×10^{20}	0.198	66.09
$NH_2(Ni) + H(Ni) \rightarrow NH_3(Ni) + Ni$	-	5.26×10^{19}	−0.201	26.08
$NH_2(Ni) + Ni \rightarrow NH(Ni) + H(Ni)$	-	5.70×10^{19}	0.174	12.21
$NH(Ni) + H(Ni) \rightarrow NH_2(Ni) + Ni$	-	9.22×10^{19}	−0.155	78.27
$NH(Ni) + Ni \rightarrow N(Ni) + H(Ni)$	-	6.11×10^{19}	0.141	28.83
$N(Ni) + H(Ni) \rightarrow NH(Ni) + Ni$	-	6.28×10^{20}	0.169	103.55

experimental and simulated NH_3 conversion results, using both original and optimized kinetic parameters, is provided in Table S2 of the supplementary material.

Table 4 presents the thermodynamically consistent set of optimized parameters for the elementary steps in the microkinetic mechanism considering Ru and Ni as active surfaces for the Ru/Ba/Ni-BCZY catalytic system. It should be noted that throughout this microkinetic study, barium is treated as a promotor [54,88,89] and its effect is implicitly reflected in the optimized Ru kinetic parameters. Although synergistic effects between two metals (Ru and Ni) can, in some cases, modify the reaction pathway or shift the rate-limiting step, such effects were not explicitly accounted for in this modeling framework. Instead, we assumed a dual-site, non-interacting surface where each metal contributes independently to the overall activity. Furthermore, this model is intended to describe the kinetics of this specific material. Parameter modifications, including changes in A, β, and Ea values, are presented in Table S1 in supplementary material.

To gather more insights on the dynamics on the surface during ammonia decomposition, the surface coverages and the gas-phase concentration of NH_3 was investigated along the length of the reactor. As demonstrated in Fig. 8, the conversion increases steadily along the reactor with increasing temperature. Furthermore, at temperatures beyond 773 K, the full length of the reactor is not required to achieve full conversion. Fig. 9 shows the simulated coverages of the key surface species along the reactor length using the proposed microkinetic model in Table 4. The coverages correspond to 615 K (dashed lines) and 818 K (solid lines), at which the 0.5Ru/1Ba/Ni-BCZY catalyst exhibits 10 % and 100 % conversion, respectively. The other parameters were set at 1 bar pressure and a gas hourly space velocity of 50,000 h^{-1} with an inlet concentration of 1000 ppm NH_3 in Ar. As seen in Fig. 9, the adsorbed NH_3 species are negligible compared to the adsorbed nitrogen and hydrogen species, suggesting that the NH_3 adsorption and subsequent hydrogen abstraction reactions are fast. Both Ru and Ni surface sites are predominantly covered by adsorbed nitrogen species throughout the reactor length at 615 K, with only a small fraction of free sites and adsorbed hydrogen species. This indicates that N_2 desorption is likely the rate limiting step, in agreement with prior studies [15,37, 90–92]. At higher temperature of 818 K (solid lines), the N_2 desorption is faster, and the adsorbed nitrogen coverages are predicted to decline along the length increasing the free surface sites. Under these operating conditions, in comparison to the active nickel sites, the adsorbed nitrogen and hydrogen species coverages on the ruthenium sites are lower, suggesting relatively higher rates of association and desorption of gaseous N_2 and H_2 on the ruthenium sites. Also, a higher accumulation of the adsorbed hydrogen species on the nickel surface is predicted, especially at higher temperature, in comparison to the ruthenium surface, which suggests that the Ni surface is more prone to hydrogen poisoning [76,93] than Ru.

In order to probe only the surface kinetics of the active ruthenium and nickel sites, without the influence of reactor geometry and transport properties, $DETCHEM^{SURFPROBE}$ was used to numerically evaluate the relative activity of the metals in terms of turnover frequency (TOF) [61] using the kinetic parameters proposed in this work (Table 4). The turnover frequencies were calculated based on the surface fluxes (Eqs. 7 and 8) and the surface site density, in the range of 450–850 K for a mole fraction of 1000 ppm of NH_3 and 1 bar pressure, and the results are shown in Fig. 10. When comparing the two catalyst surface sites individually, Ni exhibits lower TOF than Ru up to 808 K, which underscores the higher efficiency of ruthenium for ammonia decomposition.

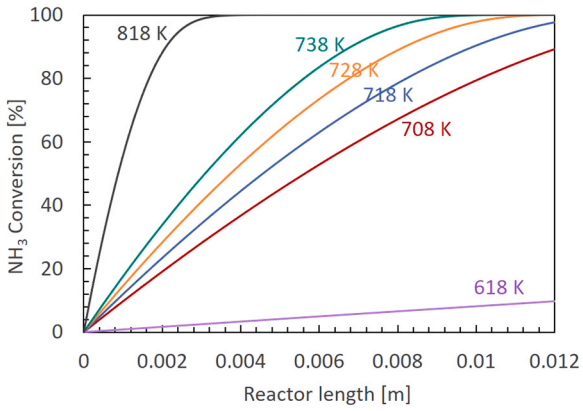

Fig. 8. Ammonia conversion along the reactor length at different packed-bed temperatures calculated by the optimized mechanism proposed in this work (Table 4). Conditions: 1000 ppm NH_3 in Ar; GSHV = 50,000 h^{-1}, P = 1 bar.

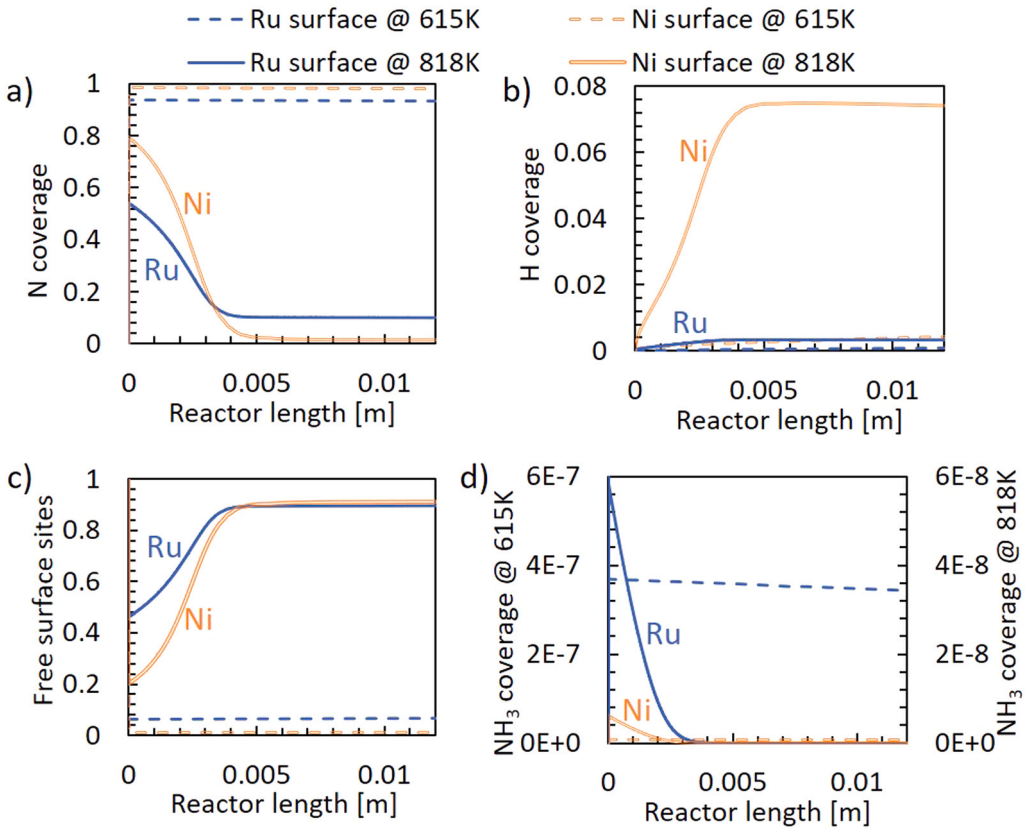

Fig. 9. Spatially resolved simulated adsorbed species coverages according to the optimized mechanism proposed in this work (Table 4). Conditions: 1000 ppm NH_3 in Ar; GHSV = 50,000 h^{-1}; P = 1 bar; T = 615 K (dashed lines) and T = 818 K (solid lines). a) N species, b) H species, c) free Ru and Ni sites, and d) NH_3 species.

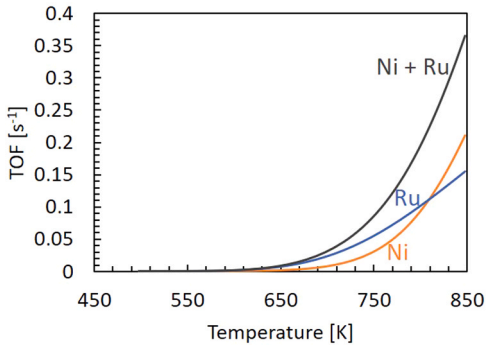

Fig. 10. Simulated turnover frequency (TOF) comparison for the Ru-based, the Ni-based and the combined model as a function of temperature. Conditions: 1000 ppm NH_3 in Ar; GHSV = 50,000 h^{-1}; P = 1 bar.

However, Ni exhibits a much stronger temperature dependency and has higher TOF values compared to Ru once the temperature exceeds 808 K. Since the combined model considers two independent surface sites, the overall TOF may be obtained by summation of the TOFs of the individual surfaces and exhibits strong temperature dependency similarly to Ni. It may be inferred that at operating temperatures below 673 K ruthenium is more efficient than nickel, and at temperatures above 673 K the bimetallic catalyst samples containing both Ni and Ru surface sites would be more efficient than monometallic ones [94]. The improved turnover frequency observed in the bimetallic system likely results from a reduction in the energy barriers of key steps, rather than a synergistic shift in the reaction pathway [37,95–97].

Using the validated microkinetic model, we performed a parametric study considering a broader range of operating conditions for ammonia decomposition in a packed-bed reactor. In Fig. 11, the effect of various operating conditions, namely the inlet feed concentrations, the total inlet flowrate, and the pressure on the predicted conversion of ammonia are shown. The left-side graphs in Fig. 11 demonstrate the simulated data at a constant temperature with varying operating conditions, while the right-side plots showcase the ammonia conversion also as a function of reactor temperature. Unless specified as variable, the parameters are T = 615 K (T_{10}), P = 1 bar, 1000 ppm NH_3 in Ar with GHSV = 50,000 h^{-1}. Fig. 11a shows the effect of varying ammonia concentration in the feed, keeping all other operating conditions constant. The model predicts an exponential decline in the ammonia conversion with increase in the ammonia concentration at the inlet in the range of 100 ppm to 10,000 ppm NH_3 inlet concentration. This also results in the activity shifting towards higher temperatures, as shown in Fig. 11b. This trend suggests that a saturation of the active sites occurs due to the increase in the ammonia concentration, leading to an increase in the overall rate [36]. A similar trend of monotonic decrease in conversion is observed when the total flowrate is increased in the range of 100–100, 000 h^{-1} (Fig. 11c and Fig. 11d). Therefore, catalyst operation at lower flowrates would lead to a better catalyst performance, even at low temperatures. It should be considered, however, that a stack of protonic ceramic cells as typically exploited in real-world applications which is a different reactor configuration than a fixed bed reactor as considered for the present study and that different flow limitations apply [98]. In contrast, the increase in the total pressure from 0.5 to 5 bar leads to a slight increase in ammonia conversion due to the increase in the contact time between the surface sites and ammonia molecules. Additionally, Fig. 11e and Fig. 11f illustrate the combined effect of temperature and pressure. At temperatures up to 613 K, the increase in pressure has a negligible effect on the obtained conversion, indicating that the system is kinetically limited. However, at 693 K, full conversion is achieved at 5 bar pressure, whereas only about 71 % conversion is achieved at 1 bar,

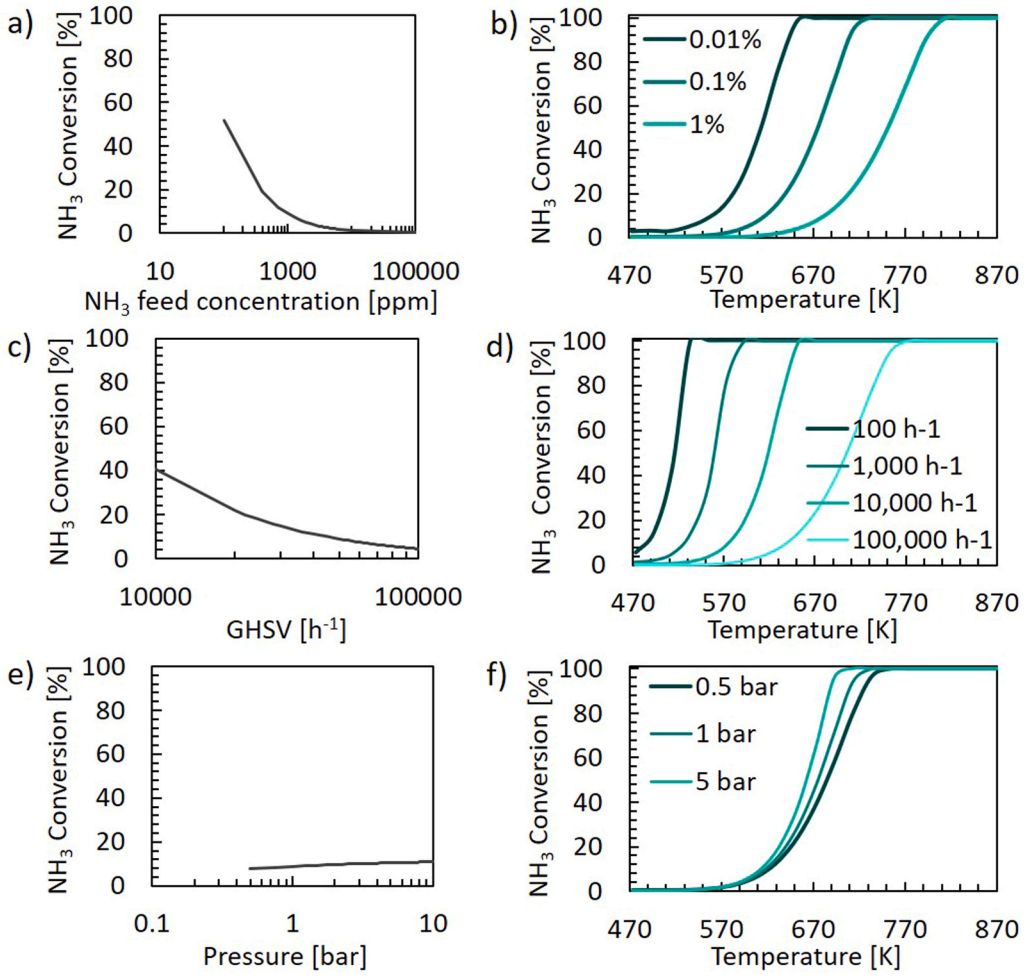

Fig. 11. Effect of varying individual operating conditions on simulated ammonia conversion using the optimized microkinetic model proposed in Table 4. The base conditions are 1000 ppm NH_3 balance in Ar with GHSV = 50,000 h^{-1} and P = 1 bar. Calculations were performed at a constant temperature of 615 K (a, c, and e), and as a function of temperature (b, d, and f). a, b) inlet ammonia concentration of 100–10,000 ppm; c, d) GHSV of 100–100,000 h^{-1}; e, f) pressure of 0.5–5 bar.

signifying a shift towards a diffusion-controlled regime. Therefore, above 613 K, the dependency on temperature becomes more pronounced, leading to better catalytic performance at higher pressures.

5. Summary and conclusion

In this study, a Ba-promoted ruthenium catalyst supported on a Ni-BCZY cermet is experimentally and numerically investigated for ammonia decomposition in a packed-bed reactor. Physisorption, SEM, EDX, and TPR techniques were employed to characterize the samples, which allowed to gain insights on the sample microstructure and quantify the active surface sites. Experimental data showcased the suitability of the 0.5 wt% Ru sample promoted with 1 wt% Ba supported on a Ni-BCZY cermet for efficient ammonia decomposition. Our investigation revealed that the presence of Ni in the support enhances the activity for NH_3 decomposition by providing additional active sites, which supports earlier findings reported in literature. However, its addition in the form of a cermet support diminishes the catalyst performance in the packed-bed, due to the decrease in porosity during the synthesis procedure used to obtain the mechanical properties necessary for fuel cell applications. Simulations performed with existing detailed kinetic models for the cermet support and the ruthenium-impregnated sample highlighted the need for optimization of the kinetic parameters in order to consider the effect of changes to support and sample morphology. Therefore, a new microkinetic model with a thermodynamically consistent set of parameters for the ruthenium and nickel surfaces are proposed and further validated with the experimental data.

Through numerical investigations with the validated microkinetic model, it was further demonstrated that the associative desorption of nitrogen is the rate limiting step that leads to the accumulation of adsorbed nitrogen species on both the ruthenium and the nickel surface sites. Analysis of the TOF over each metal surface reveals that the activity of Ni is higher than that of Ru if temperatures exceed 808 K. Therefore, the presence of Ni in the cermet material, which was added in order to increase in the proton conductivity of the cell, contributed to the overall thermochemical activity by introducing not only more active sites in general, but also due to their particularly higher activity under certain conditions. A parametric analysis of the operating conditions indicated that at low inlet ammonia concentrations, high pressure and low flowrates promote ammonia decomposition, even at low temperatures. Therefore, the 0.5Ru/1Ba/Ni-BCZY catalyst is particularly promising for use as an anode material in direct ammonia-fed protonic ceramic cells and may be explored further through electrochemical investigations. Future investigations will focus on validating the model under higher concentrations of ammonia in the inlet, including pure ammonia feeds, which are the typical operating conditions of PCC. The proposed microkinetic model may be utilized in the development and modeling of the protonic ceramic cell.

Funding sources

This work was funded by the Deutsche Forschungsgemeinschaft

(DFG, German Research Foundation) through projects SFB 1441 – Project-ID 426888090, and Project NSF-DFG Echem, Project-ID 460038541.

CRediT authorship contribution statement

Sofia Angeli: Writing – review & editing, Supervision, Resources, Project administration, Formal analysis, Data curation, Conceptualization. **Julian Dailly:** Writing – review & editing, Formal analysis. **Patrick Lott:** Writing – review & editing, Supervision, Formal analysis. **Sadaf Davari:** Writing – review & editing, Writing – original draft, Visualization, Validation, Resources, Investigation, Formal analysis, Data curation, Conceptualization. **Olaf Deutschmann:** Writing – review & editing, Supervision, Formal analysis, Conceptualization. **Tim Bastek:** Writing – review & editing, Resources. **Rinu Chacko:** Writing – review & editing, Validation, Software, Methodology, Formal analysis, Data curation, Conceptualization.

Declaration of Competing Interest

The authors declare that they have no known competing financial interests or personal relationships that could have appeared to influence the work reported in this paper.

Acknowledgements

The authors appreciate the cost-free academic license of DETCHEM™ and CaRMeN provided by omegadot software & consulting GmbH, Limburgerhof, Germany. Furthermore, we also thank Philipp Blanck, Andrea Degiacinto, and Kathrin Schäfer (ITCP, KIT) for their assistance regarding N_2-physisorption measurements. For the TPD-H_2, the authors are grateful to Dr. Andy Antzaras and Prof. Angeliki Lemonidou of Aristotle University of Thessaloniki. The authors also thank Dr. Steffen Tischer for his expertise in DETCHEM simulations. This work was funded by the Deutsche Forschungsgemeinschaft (DFG, German Research Foundation) through projects SFB 1441 – Project-ID 426888090, and Project NSF-DFG Echem, Project-ID 460038541.

Appendix A. Supporting information

Supplementary data associated with this article can be found in the online version at doi:10.1016/j.apcata.2025.120571.

Data availability

The experimental and simulation data used in this study are available in the NFDI repository under the persistent identifier (PID): https://hdl.handle.net/21.11165/4cat/b74m-m6rp.

References

[1] J.R. Rostrup-Nielsen, J. Sehested, J.K. Nørskov, Adv. Catal, in: Adv. Catal, Elsevier, 2002, pp. 65–139.
[2] J.O. Ighalo, P.B. Amama, Int. J. Hydrog. Energy 51 (2024) 688–700.
[3] S.D. Angeli, G. Monteleone, A. Giaconia, A.A. Lemonidou, Int. J. Hydrog. Energy 39 (2014) 1979–1997.
[4] O. Schmidt, A. Gambhir, I. Staffell, A. Hawkes, J. Nelson, S. Few, Int. J. Hydrog. Energy 42 (2017) 30470–30492.
[5] M. Chatenet, B.G. Pollet, D.R. Dekel, F. Dionigi, J. Deseure, P. Millet, R.D. Braatz, M.Z. Bazant, M. Eikerling, I. Staffell, P. Balcombe, Y. Shao-Horn, H. Schäfer, Chem. Soc. Rev. 51 (2022) 4583–4762.
[6] A. Çelik, A.B. Shirsath, F. Syla, H. Müller, P. Lott, O. Deutschmann, J. Anal. Appl. Pyrolysis 181 (2024) 106628.
[7] P. Lott, M.B. Mokashi, H. Müller, D.J. Heitlinger, S. Lichtenberg, A.B. Shirsath, C. Janzer, S. Tischer, L. Maier, O. Deutschmann, ChemSusChem (2022).
[8] N. Sánchez-Bastardo, R. Schlögl, H. Ruland, Ind. Eng. Chem. Res. 60 (2021) 11855–11881.
[9] J. Diab, L. Fulcheri, V. Hessel, V. Rohani, M. Frenklach, Int. J. Hydrog. Energy 47 (2022) 25831–25848.
[10] M. Mokashi, A.B. Shirsath, A. Çelik, P. Lott, H. Müller, S. Tischer, L. Maier, J. Bode, D. Schlereth, F. Scheiff, D. Flick, M. Bender, K. Ehrhardt, O. Deutschmann, Chem. Eng. J. 485 (2024) 149684.
[11] A. Çelik, I. Ben Othman, H. Müller, P. Lott, O. Deutschmann, React. Chem. Eng. 9 (2024) 108–118.
[12] A. Midilli, I. Dincer, M. Ay, Energy Policy 34 (2006) 3623–3633.
[13] E.M. Gray, Adv. Appl. Ceram. 106 (2007) 25–28.
[14] M. Hirscher, L. Zhang, H. Oh, Appl. Phys. A 129 (2023) 112.
[15] S. Mateti, L. Saranya, G. Sathikumar, Q. Cai, Y. Yao, Y. (Ian) Chen, Nanotechnology 33 (2022) 222001.
[16] D. Clematis, D. Bellotti, M. Rivarolo, L. Magistri, A. Barbucci, Energies 16 (2023) 6035.
[17] D. Cheddie, in: D. Minic (Ed.), Hydrog. Energy - Chall. Perspect, InTech, 2012.
[18] K.E. Lamb, M.D. Dolan, D.F. Kennedy, Int. J. Hydrog. Energy 44 (2019) 3580–3593.
[19] T.P. Hignett, T.P. Hignett (Eds.), Fertil. Man., Springer Netherlands, Dordrecht, 1985, pp. 73–82.
[20] C. Duan, R.J. Kee, H. Zhu, C. Karakaya, Y. Chen, S. Ricote, A. Jarry, E.J. Crumlin, D. Hook, R. Braun, N.P. Sullivan, R. O'Hayre, Nature 557 (2018) 217–222.
[21] J. Kim, S. Sengodan, S. Kim, O. Kwon, Y. Bu, G. Kim, Renew. Sustain. Energy Rev. 109 (2019) 606–618.
[22] Y. Wang, Y. Ling, B. Wang, G. Zhai, G. Yang, Z. Shao, R. Xiao, T. Li, Energy Environ. Sci. 16 (2023) 5721–5770.
[23] A. Tarutin, N. Danilov, J. Lyagaeva, D. Medvedev, Appl. Sci. 10 (2020) 2481.
[24] C. Duan, J. Huang, N. Sullivan, R. O'Hayre, Appl. Phys. Rev. 7 (2020) 011314.
[25] M. Marrony, J. Dailly, J. Electrochem. Soc. 164 (2017) F988–F994.
[26] D. Zou, Y. Yi, Y. Song, D. Guan, M. Xu, R. Ran, W. Wang, W. Zhou, Z. Shao, J. Mater. Chem. A 10 (2022) 5381–5390.
[27] K. Bae, H.-S. Noh, D.Y. Jang, J. Hong, H. Kim, K.J. Yoon, J.-H. Lee, B.-K. Kim, J. H. Shim, J.-W. Son, J. Mater. Chem. A 4 (2016) 6395–6403.
[28] G. Mather, Solid State Ion.. 162–163 (2003) 115–120.
[29] W.G. Coors, A. Manerbino, J. Membr. Sci. 376 (2011) 50–55.
[30] A. Atkinson, S. Barnett, R.J. Gorte, J.T.S. Irvine, A.J. McEvoy, M. Mogensen, S. C. Singhal, J. Vohs, Nat. Mater. 3 (2004) 17–27.
[31] J. Kim, A. Jun, O. Gwon, S. Yoo, M. Liu, J. Shin, T.-H. Lim, G. Kim, Nano Energy 44 (2018) 121–126.
[32] A.F.S. Molouk, J. Yang, T. Okanishi, H. Muroyama, T. Matsui, K. Eguchi, J. Power Sources 305 (2016) 72–79.
[33] C. Sikalidis, Synthesis and characterization, processing and specific applications. Advances in Ceramics, InTech, 2011.
[34] J. Tong, D. Clark, M. Hoban, R. O'Hayre, Solid State Ion.. 181 (2010) 496–503.
[35] F. Dawood, M. Anda, G.M. Shafiullah, Int. J. Hydrog. Energy 45 (2020) 3847–3869.
[36] S. Davari, C. Cárdenas, M. Hettel, P. Lott, S. Tischer, S. Angeli, O. Deutschmann, Chem. Ing. Tech. 96 (2024) 1735–1750.
[37] I. Lucentini, X. Garcia, X. Vendrell, J. Llorca, Ind. Eng. Chem. Res. 60 (2021) 18560–18611.
[38] G. Papapolymerou, V. Bontozoglou, J. Mol. Catal. Chem. 120 (1997) 165–171.
[39] C. Liang, W. Li, Z. Wei, Q. Xin, C. Li, Ind. Eng. Chem. Res. 39 (2000) 3694–3697.
[40] Z. Su, J. Guan, Y. Liu, D. Shi, Q. Wu, K. Chen, Y. Zhang, H. Li, Int. J. Hydrog. Energy 51 (2024) 1019–1043.
[41] S.F. Yin, B.Q. Xu, X.P. Zhou, C.T. Au, Appl. Catal. Gen. 277 (2004) 1–9.
[42] F. Schüth, R. Palkovits, R. Schlögl, D.S. Su, Energy Env. Sci. 5 (2012) 6278–6289.
[43] J.K. Nørskov, T. Bligaard, A. Logadottir, S. Bahn, L.B. Hansen, M. Bollinger, H. Bengaard, B. Hammer, Z. Sljivancanin, M. Mavrikakis, Y. Xu, S. Dahl, C.J. H. Jacobsen, J. Catal. 209 (2002) 275–278.
[44] W. Yan, B. Liang, G. Bi, H. Zhuo, W. Wang, H. Duan, G. Xu, F. Wang, Y. Su, T. Zhang, X. Yang, Y. Huang, ACS Sustain. Chem. Eng. 12 (2024) 15024–15032.
[45] B. Teng, C. Ma, J. Chen, Y. Zhang, B. Wei, M. Sang, H. Wang, Y. Sun, ACS Appl. Nano Mater. 7 (2024) 15012–15024.
[46] A. Porta, C.G. Visconti, L. Castoldi, R. Matarrese, C. Jeong-Potter, R. Farrauto, L. Lietti, Appl. Catal. B Environ. 283 (2021) 119654.
[47] K. Yamazaki, M. Matsumoto, M. Ishikawa, A. Sato, Appl. Catal. B Environ. 325 (2023) 122352.
[48] T. Weissenberger, R. Zapf, H. Pennemann, G. Kolb, Catalysts 14 (2024) 104.
[49] J. Shin, U. Jung, J. Kim, K.D. Kim, D. Song, Y. Park, B.-S. An, K.Y. Koo, Appl. Catal. B Environ. 340 (2024) 123234.
[50] Y. Im, H. Muroyama, T. Matsui, K. Eguchi, Int. J. Hydrog. Energy 47 (2022) 32543–32551.
[51] R. Shao, L. Zhang, L. Wang, J. Wang, X. Zhang, S. Han, X. Cheng, Z. Wang, Int. J. Hydrog. Energy 68 (2024) 311–320.
[52] V. Cechetto, L. Di Felice, J.A. Medrano, C. Makhloufi, J. Zuniga, F. Gallucci, Fuel Process. Technol. 216 (2021) 106772.
[53] M.E.E. Abashar, Y.S. Al-Sughair, I.S. Al-Mutaz, Appl. Catal. Gen. 236 (2002) 35–53.
[54] Z. Zhang, C. Karakaya, R.J. Kee, J.D. Way, C.A. Wolden, ACS Sustain. Chem. Eng. 7 (2019) 18038–18047.
[55] J.C. Ganley, F.S. Thomas, E.G. Seebauer, R.I. Masel, Catal. Lett. 96 (2004) 117–122.
[56] T.E. Bell, L. Torrente-Murciano, Top. Catal. 59 (2016) 1438–1457.
[57] T.V. Choudhary, C. Sivadinarayana, D.W. Goodman, Catal. Lett. 72 (2001) 197–201.
[58] J. Dailly, G. Taillades, M. Ancelin, P. Pers, M. Marrony, J. Power Sources 361 (2017) 221–226.
[59] G. Ertl, H. Knözinger, J. Weitkamp (Eds.), Handbook of Heterogeneous Catalysis, 1st ed., Wiley, 1997.

[60] P. Lott, P. Dolcet, M. Casapu, J.-D. Grunwaldt, O. Deutschmann, Ind. Eng. Chem. Res. 58 (2019) 12561–12570.
[61] O. Deutschmann, S. Tischer, S. Kleditzsch, V. Janardhanan, C. Correa, D. Chatterjee, N. Mladenov, D. Minh, H, H. Karadeniz, M. Hettel, V. Menon, A. Banerjee, H. Gossler, A. Shirsath, E. Daymo, DETCHEM (n.d.).
[62] A.S. Pushnov, Chem. Pet. Eng. 42 (2006) 14–17.
[63] H. Gossler, L. Maier, S. Angeli, S. Tischer, O. Deutschmann, Phys. Chem. Chem. Phys. 20 (2018) 10857–10876.
[64] H. Gossler, L. Maier, S. Angeli, S. Tischer, O. Deutschmann, Catalysts 9 (2019) 227.
[65] A. Cao, V.J. Bukas, V. Shadravan, Z. Wang, H. Li, J. Kibsgaard, I. Chorkendorff, J. K. Nørskov, Nat. Commun. 13 (2022) 2382.
[66] A. Boisen, S. Dahl, J. Norskov, C. Christensen, J. Catal. 230 (2005) 309–312.
[67] M. Hattori, S. Iijima, T. Nakao, H. Hosono, M. Hara, Nat. Commun. 11 (2020) 2001.
[68] K. Ooya, J. Li, K. Fukui, S. Iimura, T. Nakao, K. Ogasawara, M. Sasase, H. Abe, Y. Niwa, M. Kitano, H. Hosono, Adv. Energy Mater. 11 (2021) 2170018.
[69] K. Honkala, A. Hellman, I.N. Remediakis, A. Logadottir, A. Carlsson, S. Dahl, C. H. Christensen, J.K. Nørskov, Science 307 (2005) 555–558.
[70] O. Hinrichsen, F. Rosowski, A. Hornung, M. Muhler, G. Ertl, J. Catal. 165 (1997) 33–44.
[71] H. Zhu, C. Karakaya, R.J. Kee, Int. J. Green. Energy 19 (2022) 1568–1582.
[72] R. Chacko, K. Keller, S. Tischer, A.B. Shirsath, P. Lott, S. Angeli, O. Deutschmann, J. Phys. Chem. C. 127 (2023) 7628–7639.
[73] A.B. Mhadeshwar, H. Wang, D.G. Vlachos, J. Phys. Chem. B 107 (2003) 12721–12733.
[74] K. Delgado, L. Maier, S. Tischer, A. Zellner, H. Stotz, O. Deutschmann, Catalysts 5 (2015) 871–904.
[75] Y. Lin, R. Ran, Y. Guo, W. Zhou, R. Cai, J. Wang, Z. Shao, Int. J. Hydrog. Energy 35 (2010) 2637–2642.
[76] K. Miyazaki, H. Muroyama, T. Matsui, K. Eguchi, Sustain. Energy Fuels 4 (2020) 5238–5246.
[77] S.T. Aruna, M. Muthuraman, K.C. Patil, Solid State Ion.. 111 (1998) 45–51.
[78] T. Shimonosono, T. Ueno, Y. Hirata, J. Asian Ceram. Soc. 7 (2019) 20–30.
[79] Y. Liu, Z. Shao, T. Mori, S.P. Jiang, Mater. Rep. Energy 1 (2021) 100003.
[80] K. Aika, Catal. Today 286 (2017) 14–20.
[81] C. Chatzilias, E. Martino, S. Tsatsos, G. Kyriakou, A. Katsaounis, C.G. Vayenas, Chem. Eng. J. 430 (2022) 132967.
[82] G. Bergeret, P. Gallezot, in: G. Ertl, H. Knözinger, F. Schüth, J. Weitkamp (Eds.), Handb. Heterog. Catal, 1st ed., Wiley, 2008, pp. 738–765.
[83] J. Yang, A.F.S. Molouk, T. Okanishi, H. Muroyama, T. Matsui, K. Eguchi, ACS Appl. Mater. Interfaces 7 (2015) 7406–7412.
[84] P. Forzatti, L. Lietti, Catal. Today 52 (1999) 165–181.
[85] C.A. Schneider, W.S. Rasband, K.W. Eliceiri, Nat. Methods 9 (2012) 671–675.
[86] G. Bergeret, P. Gallezot, in: G. Ertl, H. Knözinger, F. Schüth, J. Weitkamp (Eds.), Handb. Heterog. Catal, 1st ed., Wiley, 2008, pp. 738–765.
[87] K. Okura, K. Miyazaki, H. Muroyama, T. Matsui, K. Eguchi, RSC Adv. 8 (2018) 32102–32110.
[88] N. Shimoda, Y. Kimura, Y. Kobayashi, J. Kubota, S. Satokawa, Int. J. Hydrog. Energy 42 (2017) 29745–29755.
[89] Z. Wang, B. Liu, J. Lin, Appl. Catal. Gen. 458 (2013) 130–136.
[90] Y. Qiu, F.S. Franchi, N. Usberti, A. Beretta, Fuel Process. Technol. 276 (2025) 108270.
[91] P.K. Yadav, S. Gunge, A.S. Russel, G. Deo, Appl. Catal. B Environ. Energy 371 (2025) 125205.
[92] S.R. Kulkarni, N. Realpe, A. Yerrayya, V.K. Velisoju, S. Sayas, N. Morlanes, J. Cerillo, S.P. Katikaneni, S.N. Paglieri, B. Solami, J. Gascon, P. Castaño, Catal. Sci. Technol. 13 (2023) 2026–2037.
[93] J. Zhang, H. Xu, W. Li, Appl. Catal. Gen. 296 (2005) 257–267.
[94] I. Lucentini, G. García Colli, C.D. Luzi, I. Serrano, O.M. Martínez, J. Llorca, Appl. Catal. B Environ. 286 (2021) 119896.
[95] D.A. Hansgen, D.G. Vlachos, J.G. Chen, Nat. Chem. 2 (2010) 484–489.
[96] S. Zhou, Y. Liu, L. Cheng, T.T. Isimjan, J. Tian, X. Yang, Inorg. Chem. Front 11 (2024) 5244–5253.
[97] I. Lucentini, A. Casanovas, J. Llorca, Int. J. Hydrog. Energy 44 (2019) 12693–12707.
[98] Y.D. Akenteng, X. Yang, Y. Zhao, A. Lysyakov, A. Matveev, D. Chen, Ionics 28 (2022) 3367–3378.